Co–Mn-oxide spinel catalysts for CO and propane oxidation at mild temperature

Benjamin Faure faure.benjamin.n@gmail.com, Pierre Alphonse [*]

CIRIMAT-UPS, Université de Toulouse, 118 route de Narbonne 31062 Toulouse cedex 09, France

ABSTRACT

$Co_xMn_{3-x}O_4$ oxides ($0 \leq x \leq 3$) were prepared by controlled decomposition of mixed oxalates near 200 °C, followed by a calcination at 300 °C. These oxides are amorphous for $x < 0.9$. For higher cobalt fraction they have a cubic spinel structure and their crystallite size grows with the cobalt fraction. These materials have a large surface area; the highest values, exceeding $250\,m^2/g$, were obtained for $x \approx 2$. The spinel oxides exhibit an outstanding catalytic activity for propane oxidation at mild temperature (20–200 °C). They are also active for CO oxidation at ambient temperature. This high activity was correlated both with the surface area and the cobalt concentration. The most efficient material is $Co_{2.3}Mn_{0.7}O_4$, which has a better activity than cobalt oxide catalysts reported in the literature.

© 2015 Elsevier B.V. All rights reserved.

1. Introduction

Catalytic oxidation is a very effective method for the abatement of low concentrations of Volatile Organic Compounds (VOCs). Currently, the most active catalysts are supported noble metals [1–3]. However these catalysts are very expensive and their activity can be strongly inhibited by CO [4], water or chloride [5]. For low temperature applications, like VOCs removal in indoor air, precious metals can be replaced by transition metal oxides [6]. Especially spinel cobalt oxide (Co_3O_4) was reported to be the best catalyst for the total oxidation of CO [7] and hydrocarbons [6,8]. Spinel oxides, with the general formula AB_2O_4, contain cation sites of different coordination (tetrahedral and octahedral) with the oxide anions arranged in a cubic close-packed lattice. Partial substitution of cobalt by manganese gives mixed Co–Mn spinel oxides, which can be better catalysts than Co_3O_4 for the oxidation of VOCs [9–11].

Most often the catalysts reported in the literature are synthesized at high temperature (>500 °C). This requirement, unavoidable for automotive catalytic converters, becomes useless for VOCs abatement at mild temperature (<300 °C). Actually it is expected that metastable nanocrystalline oxides, with very large porosity and surface area, will be highly active catalysts. This kind of materials can be easily obtained by thermal decomposition of metal oxalates. Indeed a close control of the decomposition allows preparing mixed oxides with very high surface area (300–500 m^2/g) [12,13]. Moreover this easy and inexpensive method is also very convenient to obtain mixed oxides [14].

The goal of this study was the synthesis of large surface area $Co_xMn_{3-x}O_4$ oxides ($0 \leq x \leq 3$) by controlled decomposition of mixed oxalates and the evaluation of the catalytic performance of these metastable materials for the total oxidation of carbon monoxide and propane at mild temperature (20–200 °C). Carbon monoxide is produced in large amount by transportation, industrial and domestic activities. It is extremely toxic and catalytic oxidation into CO_2 constitutes the best solution for CO removal from indoor air [7]. Thus low cost, precious metal free catalysts, working at room temperature are highly demanded. Propane is largely used as domestic and industrial fuel. Besides it is also the third most common motor vehicle fuel in the world behind gasoline and Diesel fuel. On the other hand it is generally admitted that alkanes are the least reactive among VOCs and a catalyst able to remove propane at mild temperatures is expected to be active for other VOCs as well.

2. Experimental

2.1. Synthesis of oxides

2.1.1. Preparation of mixed oxalates

Mixed oxalates $Co_{x/3}Mn_{(3-x)/3}C_2O_4 \cdot 2H_2O$ were precipitated at room temperature by quick introduction of an aqueous solution of cobalt and manganese nitrates (200 mL; 0.2 M) into an aqueous solution of ammonium oxalate (200 mL; 0.22 M) under vigor-

ous stirring. After 30 min, the precipitate was filtered, thoroughly washed with deionized water and dried in air at 70 °C.

2.1.2. Thermal decomposition of oxalates

The thermal decomposition of oxalates was carried out in a vertical tubular fixed-bed flow reactor under atmospheric pressure. The internal diameter of reactor was 1 cm. The flow rate of the inlet gas (4% O_2 in Ar) was 100 cm^3/min. The outlet gas composition was followed using a mass spectrometer (HPR20-QIC from Hiden Analytical). The temperature of the reacting solid was recorded by a K thermocouple positioned inside the powdered sample. This setup allowed controlling both the temperature of the reacting material and the composition of the atmosphere. The temperature was increased at 2.5 °C/min until CO_2 emission was detected; from then the decomposition was done in isothermal conditions. For example, in the case of manganese oxalate this temperature was about 210 °C. When CO_2 emission was over, to ensure a total decomposition, even in the core of particles, the partial pressure of O_2 was augmented gradually to 20%; then the temperature was increased at 5 °C/min up to 300 °C and maintained to this value for 1 h.

2.2. Thermal analysis (TGA-DSC)

The thermal decomposition of oxalates was studied by thermogravimetric analysis (TGA) and differential scanning calorimetry (DSC), using a constant heating rate (5 °C/min), on a TGA-DSC-1 Mettler–Toledo device in the temperature range 30–600 °C. The flowing gas was a mixture 20% O_2 in Ar. About 5 mg of oxalate powder were placed in a 40 mL aluminium pan and the reference was an empty aluminium pan.

2.3. Powder X-ray diffraction (PXRD)

The crystal structure was investigated via powder X-ray diffraction. Data was collected, at room temperature, with a Bruker AXS D4 θ–2θ diffractometer, in the Bragg–Brentano geometry, using filtered Cu Kα radiation and a graphite secondary-beam monochromator. Diffraction intensities were measured by scanning from 20 to 80° (2θ) with a step size of 0.02° (2θ).

A quantitative estimation of the lattice parameters and peak broadening was accomplished by profile fitting of the whole XRD patterns using the Fullprof software [15]. The peak profiles were modeled by Thompson-Cox-Hastings [16] pseudo-Voigt functions. The parameters refined were zero shift (2θ), background, cell parameters and peak shape. The size and strain contribution to the integral breadth of each reflection were calculated by the software. The instrumental broadening contribution was evaluated by using an α-alumina sample (NIST Standard Reference Material 1976b).

The structural changes versus temperature were followed by High Temperature X-ray Diffraction (HTXRD) with a Bruker AXS D8 diffractometer (using Ni-filtered Cu Kα radiation) equipped with a high temperature chamber Anton Paar HTK1200N. Diffraction intensities were recorded in synthetic air flow (20% O_2 in N_2), at fixed temperature, every 10 °C, in the range 100–500 °C. The heating rate between each step was 10 °C/min. The time needed to record each pattern was about 15 min.

2.4. Specific surface area, pore size distribution

Specific surface area and pore size distribution were calculated from nitrogen adsorption-desorption isotherms collected at 77 K, using an adsorption analyzer (Micromeritics Tristar II 3020). The specific surface areas were computed from adsorption isotherms, using the Brunauer–Emmett–Teller (BET) method [17]. The pore size distributions (PSD) were computed from desorption isotherms

by the NLDFT method [18] (with Quantachrome Autosorb-1 software using silica equilibrium transition kernel at 77K, based on a cylindrical pore model).

Pore volume (V_{pore}) was calculated from the adsorbed volume at a relative pressure of 0.995 (V_{sat}) by:

$$V_{pore} = \frac{N_2 \text{ gas density}}{N_2 \text{ liq. density}} V_{sat} = 0.00155 \, V_{sat}$$

Prior to analysis, to remove the species adsorbed on the surface, the oxalate samples (about 0.5 g) were degassed for 16 h at 70 °C whereas the oxide samples (about 0.1 g) were degassed for 16 h at 90 °C (final pressure <10^{-3} Pa).

2.5. Electron microscopy

Transmission electron microscopy analyses were performed with a Jeol JEM-1400 operating at 80 kV. Samples were prepared by putting a drop of an ethanol suspension of particles on a carbon-coated copper grid.

Scanning electron microscopy analyses were performed with a SEM FEG FEI Quanta-250 at 20 kV. The samples were prepared by putting a drop of an ethanol suspension of particles on an aluminum sample holder. Before analysis, the samples were covered with a thin layer (5 nm) of Pt by sputter coating.

2.6. Chemical analysis by X-ray fluorescence

The elemental composition was determined on powder samples by X-ray fluorescence with a Bruker S2 Ranger working with a maximum voltage of 50 kV and a current of 2 mA.

2.7. Catalytic tests

The activities of catalysts were tested for CO and C_3H_8 total oxidation. These tests were performed, at ambient pressure, in a tubular fixed bed flow glass reactor (internal diameter = 6 mm). The catalyst mass was always close to 0.05 g. The catalyst powder was packed in the tube giving a 2–3 mm bed length. The volumetric flow rate was 1.63 mL s^{-1} giving a contact time of 0.03 s. The size of catalyst particles was about 10 μm. The reactor operates at differential conditions only for propane oxidation, at mild temperatures (conversion <10%). The reactants were dosed by mass flow controllers (Brooks 5850). The catalyst temperature was controlled by a K-type thermocouple positioned inside the catalyst bed. For CO oxidation the temperature range was 30–200 °C and the inlet gas composition was 0.8% CO + 20% O_2 in Ar. For C_3H_8 oxidation the temperature range was 30–300 °C and the inlet gas composition was 0.4% C_3H_8 + 20% O_2 in Ar. The catalyst temperature was increased at a heating rate of 200 °C/h. The gas phase composition during the tests was monitored by mass spectrometry (HPR20-QIC from Hiden Analytical). Before the CO oxidation test, the catalysts were first pretreated with 20% O_2 in Ar for 60 min at 200 °C. The C_3H_8 oxidation test was done after CO test without any pretreatment.

3. Results and discussion

3.1. Characterization of oxalate precursors

3.1.1. XRD

The XRD pattern (Fig. 1) of manganese oxalate corresponds to the monoclinic structure with the space group C2/c (PDF # 00-025-0544) whereas cobalt oxalate has the orthorhombic structure with the space group Cccm (PDF # 00-025-0250). The structure of mixed Co–Mn oxalates depends on their manganese content. For oxalates containing more Mn than Co, pattern matching with the monoclinic
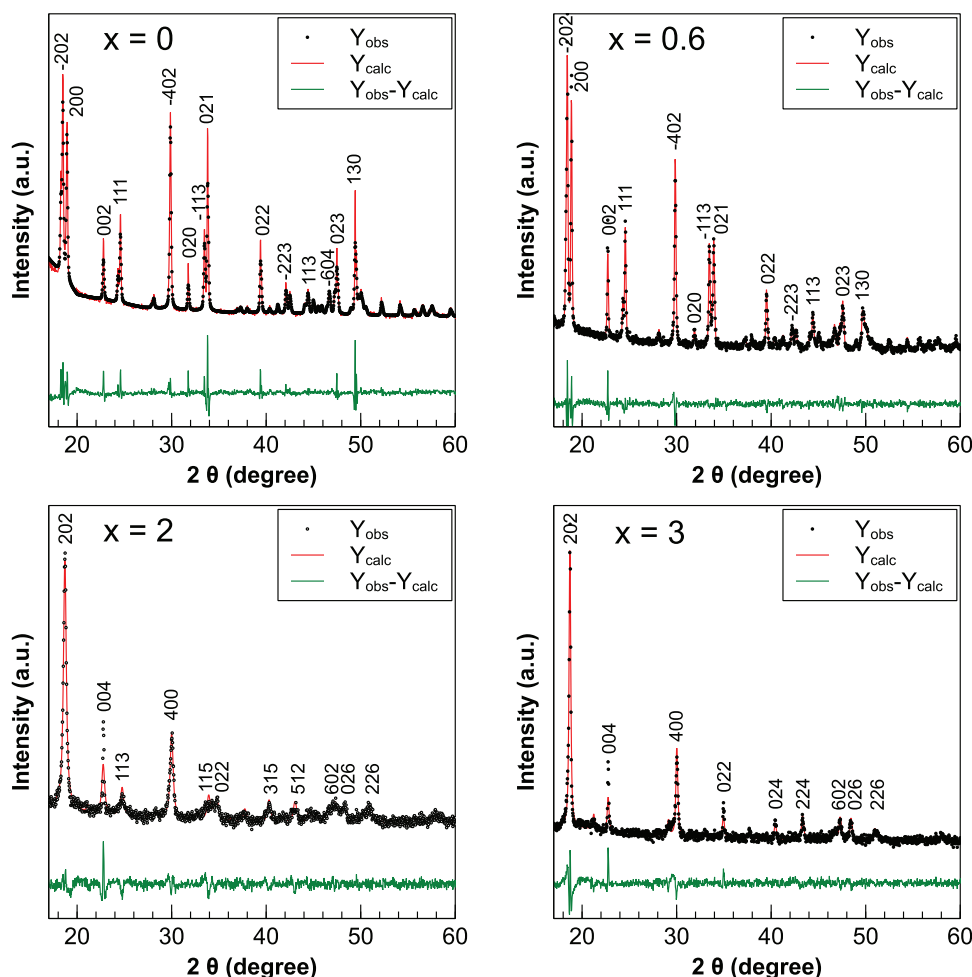
Fig. 1. Examples of XRD patterns of $Co_{x/3}Mn_{(3-x)/3}C_2O_4.2H_2O$ after the profile fitting with the FULLPROF software [15]. The upper patterns were indexed for the monoclinic structure (PDF # 00-025-0544) whereas the lower patterns were indexed for the orthorhombic structure (PDF # 00-025-0250).

Table 1
Structure parameters of $Co_{x/3}Mn_{(3-x)}/3C_2O_4.2H_2O$ determined by profile fitting of XRD patterns with FULLPROF software [15]. D is the crystallite size.

x	Space group	a (nm)	b (nm)	c (nm)	β (°)	D (nm)
0	C2/c	1.200	0.565	0.998	128.3	52
0.6	C2/c	1.197	0.561	0.996	128.2	55
0.9	C2/c	1.194	0.557	0.996	128.1	51
1.6	Cccm	1.192	0.550	1.556	90	15
2.0	Cccm	1.188	0.545	1.557	90	17
2.3	Cccm	1.191	0.546	1.564	90	21
3	Cccm	1.187	0.542	1.557	90	32

Table 2
BET surface area (S_{BET}) and pore volume (V_{pore}) of $Co_{x/3}Mn_{(3-x)/3}C_2O_4.2H_2O$ determined from N_2 adsorption isotherms at 77 K.

x	S_{BET} (m²/g)	C_{BET}	V_{pore} (cm³/g)
0	26 ± 2	130	0.095 ± 0.008
0.6	2.4 ± 0.2	120	0.010 ± 0.001
0.9	4.0 ± 0.3	130	0.030 ± 0.002
1.6	5.0 ± 0.4	150	0.062 ± 0.005
2.0	4.4 ± 0.3	110	0.044 ± 0.003
2.3	6.0 ± 0.5	160	0.074 ± 0.005
3	4.0 ± 0.3	170	0.024 ± 0.002

structure gives a better agreement whereas, when Co equals or exceeds Mn, a best fit is obtained with orthorhombic structure. The lattice parameters and the crystallite size are reported in Table 1. Both a and b lattice parameters decrease when the proportion of Co increases indicating that the smaller Co^{2+} ions ($r = 89$ pm HS) substitute for the larger Mn^{2+} ions ($r = 97$ pm HS). The crystallite size is constant, at about 50 nm, for the monoclinic structure and drops near 20 nm when the structure becomes orthorhombic. However the crystallite size of cobalt oxalate is larger, at about 30 nm, than that of Co-rich mixed oxalates.

3.1.2. Scanning electron microscopy

The SEM images for several compositions are shown in Fig. 2. The particle morphology changes according to the chemical com-

position. The particles of manganese rich oxalates (upper images) are very irregular in size and shape whereas the particles of cobalt rich oxalates are more uniform. These particles are at least ten times larger than the crystallite size determined from XRD. For $2 \leq x < 3$ the particles aggregate in ball-shaped units (lower left image). We did not observe such aggregates for cobalt oxalate, which gives rod like particles (lower right image).

3.1.3. Specific surface area and pore volume

The BET surface area (S_{BET}) and pore volume (V_{pore}) of oxalates are reported in Table 2. The surface areas of all the compounds containing cobalt are similar, in the range 4–6 m²/g. They are at least 5 times lower than the surface area of manganese oxalate which has also the largest pore volume. For this oxalate we suspected that the
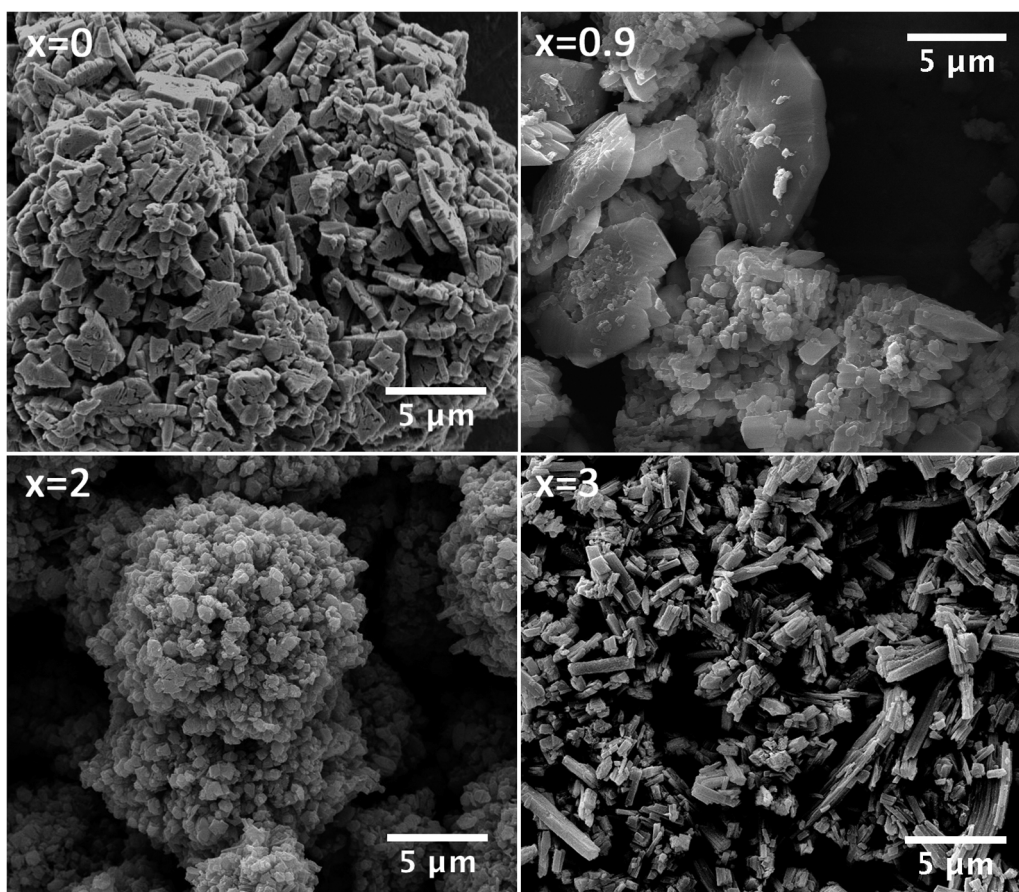
Fig. 2. SEM images of some oxalates.

degassing procedure (16 h at 70 °C in vacuum) induced the beginning of dehydration because the onset temperature of dehydration was lower than for mixed oxalates (see Section 3.2.1). Nevertheless doubling the evacuation time did not change significantly the textural properties.

3.2. Decomposition of oxalate precursors

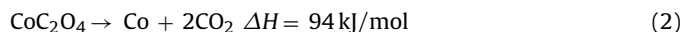#### 3.2.1. Thermal analysis of oxalate decomposition

The TGA-DSC analysis curves for several compositions are plotted in Fig. 3. The decomposition occurs in two main separated stages: below 200 °C the endothermic dehydration giving the anhydrous oxalate, followed by the exothermic decomposition near 300 °C. For an oxalate containing $2H_2O$ per mole, the mass loss due to dehydration must decrease slightly from 20.1% for $x = 0$ to 19.7% for $x = 3$. We obtain the expected value for manganese oxalate whereas the mass loss is only 19% for cobalt oxalate, indicating a number of water molecules slightly less than 2. Besides, for cobalt oxalate, the endothermic dehydration peak has a small shoulder on the right side equivalent to about 10% of the whole area. This peak is always present whatever the mass of sample analyzed or the heating rate. It could be the indication that we have a mixture between the orthorhombic form and a small amount of the monoclinic polymorph with the space group C2/c (PDF # 00-025-0251) not detected on the XRD patterns.

Thermal decomposition of transition metal oxalates hydrates has been studied for many years [19–33]. It was observed that the decomposition product for these oxalates depends on the reducibility of the metallic cation involved [23,25,32]. With cations
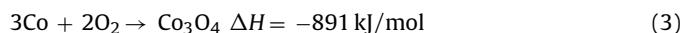
presenting a low reducibility, like Mn^{2+}, the decomposition leads to the metal oxide following the reaction:

$$MnC_2O_4 \rightarrow MnO + CO + CO_2 \quad \Delta H = 151 \, kJ/mol \tag{1}$$

Whereas for more reducible cations like Co^{2+} the decomposition produces the metal:

$$CoC_2O_4 \rightarrow Co + 2CO_2 \quad \Delta H = 94 \, kJ/mol \tag{2}$$

However in air, Co is oxidized in Co_3O_4:

$$3Co + 2O_2 \rightarrow Co_3O_4 \quad \Delta H = -891 \, kJ/mol \tag{3}$$

Similarly MnO will be also oxidized in air. According to the reaction conditions the product was reported as Mn_3O_4 [34], Mn_2O_3 [22,35], MnO_2 [26] or amorphous MnO_x [36].

Moreover the manganese or cobalt oxides formed are known to be good catalysts for the CO oxidation [7]:

$$CO + 1/2O_2 \rightarrow CO_2 \quad \Delta H = -283 \, kJ/mol \tag{4}$$

Therefore, since these oxidation reactions are very exothermic, the overall decomposition reaction is largely exothermic too.

The effect of cobalt fraction on some characteristics of mixed oxalate dehydration and decomposition is illustrated in Fig. 4. Four features are followed, the onset temperature of dehydration (T_i), the width of the decomposition peak (in °C), the enthalpy of dehydration and the enthalpy of decomposition. The upper-left plot shows that the T_i of mixed oxalates is close to the T_i of cobalt oxalate (130 °C) whereas the dehydration of Mn oxalate begins at least 30 °C below. The lower-left plot shows that the enthalpy of dehydration is rather similar for all the samples analyzed, at
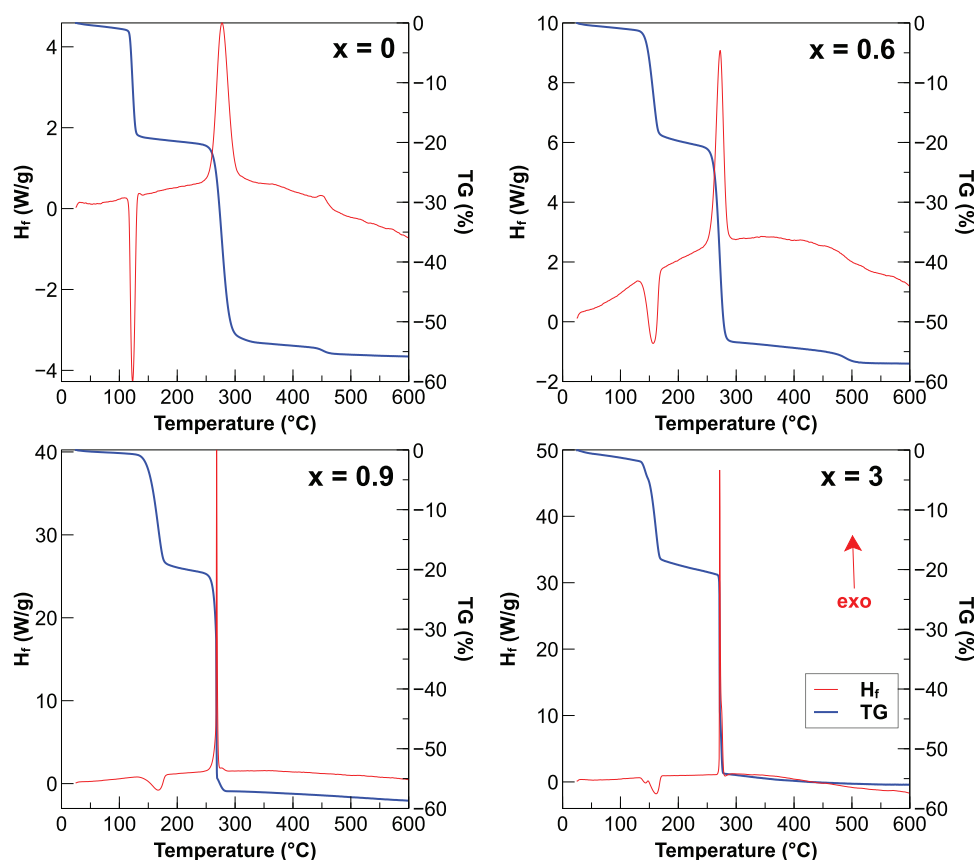
Fig. 3. TGA-DSC curves for some oxalates.

about 520 J/g (95 kJ/mol oxalate); only the enthalpy observed for manganese oxalate is slightly lower. This value is very close to the enthalpy reported by Maciejewski et al. [30].

We observed that the onset temperature of decomposition augments linearly with the cobalt content of oxalates, going from 230 °C for manganese oxalate to 255 °C for cobalt oxalate. The upper-right plot shows that the width of the decomposition peak, which is linked to the rate of the reaction, markedly decreases when the proportion of cobalt increases. Nevertheless the enthalpy of decomposition, estimated by integration of the exothermic peak, does not rise much with the cobalt fraction as shown by the lower-right plot. This is confirmed by the red line in this plot, which corresponds to the values calculated from thermodynamic data ($\Delta_f H°_{298}$) [37,38] assuming the formation of an ideal solid solution having the spinel structure (cf. § 3.2.2). Therefore we think that the increase of the decomposition rate with the proportion of cobalt could be explained by the very high reactivity of metal cobalt in oxygen containing atmospheres. Thus to avoid a temperature overshoot, leading to a fast growth of crystallites, the decomposition of cobalt-rich oxalates shall be performed in isothermal condition and low oxygen partial pressure.

3.2.2. HT-XRD of oxalate decomposition

The thermal decomposition of the oxalates was also followed by HT-XRD. The samples were heated by step of 10 °C at 5 °C/min. Taking into account the time required to record each pattern, the heating rate on the average was about 0.5 °C/min. Thus, compared with TGA-DSC for which the heating rate was 5 °C/min, a peak shift toward lower temperature can be expected.

The relevant XRD patterns for several compositions are plotted in Fig. 5. The upper-left chart corresponds to manganese oxalate.

The first pattern, recorded at 150 °C, corresponds to the anhydrous oxalate which has an orthorhombic structure with the space group Pmna (PDF # 00-032-0646). This anhydrous oxalate decomposes from 230 °C to give an amorphous phase which crystallizes only at 400 °C in cubic Mn_2O_3 (bixbyite) with the space group Ia3 (PDF # 00-041-1442). This transformation gives a small exothermal peak together with a slight mass loss at 450 °C on the TGA-DSC plot (see Fig. 3, $x = 0$).

The upper-right plot corresponds to the mixed oxalate $Co_{0.2}Mn_{0.8}C_2O_4.2H_2O$ ($xCo = 0.6$). The anhydrous oxalate pattern is observed from 140 °C. Like for manganese oxalate, this anhydrous oxalate decomposes from 220 °C to give an amorphous phase which crystallizes at 450 °C in a tetragonally deformed spinel (space group I41/amd) like Mn_3O_4 (hausmannite, PDF # 00-024-0734). Mn_3O_4 is a "normal" spinel because all Mn^{3+} cations are located in the octahedral sites, giving the cation distribution $Mn^{2+}[Mn^{3+}]_2O_4$ [39]. Bordeneuve et al. [40], from neutron diffraction data recorded on $Co_xMn_{3-x}O_4$ ceramics, showed that, for $x < 1$, the substitution occurs only in the tetrahedral site where Co^{2+} replaces Mn^{2+}.

The deformation of the cubic spinel structure is correlated with a distortion of the coordination octahedron around Mn^{3+}, usually interpreted as a consequence of the cooperative Jahn–Teller effect [41].

The lattice parameters of hausmannite are $a = 0.576$ nm and $c = 0.944$ nm [41]. Profile matching (using FullProf software [15]) gives $a = 0.575$ nm and $c = 0.938$ nm for the pattern recorded at 450 °C and $a = 0.576$ nm and $c = 0.938$ nm for the pattern recorded at 500 °C. The lower c value in our samples could originate from partial oxidation of Mn^{3+} into non-distorting Mn^{4+} in the octahedral sites because, in hausmannite structure, the coordination octahedron around Mn^{3+} are elongated approximately parallel to [001].
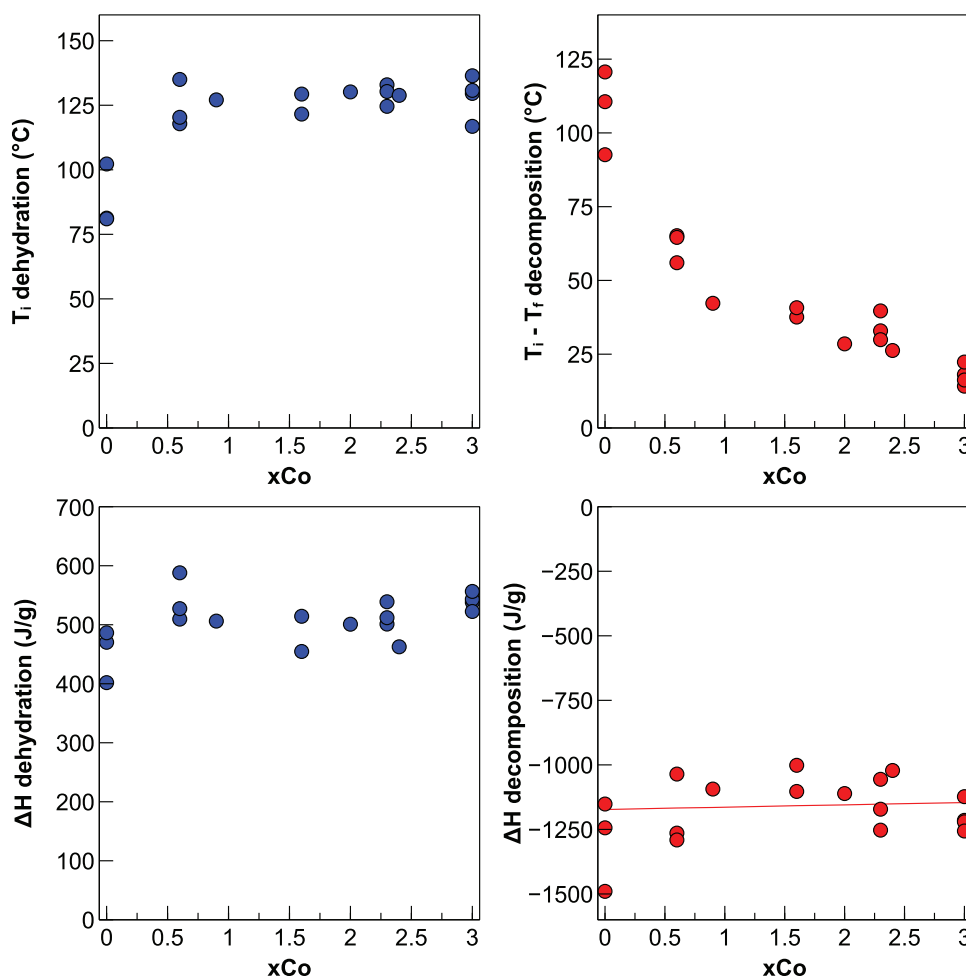
Fig. 4. Effect of cobalt fraction on the onset temperature of dehydration T_i (upper-left), the width of the decomposition peak (upper-right), the enthalpy of dehydration (lower-left) and the enthalpy of decomposition (lower-right).

Profile matching also provides an estimation of the crystallite size D; we found $D=12$ nm for $450\,^{\circ}$C and $D=14$ nm for $500\,^{\circ}$C.

It is worth noticing that the crystallization observed at $450\,^{\circ}$C is associated with a small mass loss on TG curve but, unlike manganese oxalate, gives no detectable thermal event (Fig 3, $x=0.6$). This could be an indication that, in this case, the crystallization involves only little change in the structural arrangement of atoms, because the amorphous state has a proto-spinel structure as it was previously assumed for nickel manganite spinels prepared by low temperature decomposition of mixed oxalates [42].

The lower-left plot corresponds to the mixed oxalate $Co_{0.3}Mn_{0.7}C_2O_4.2H_2O$ ($x=0.9$). The dehydration occurs above $130\,^{\circ}$C giving a compound with a XRD pattern similar to the monoclinic cobalt oxalate with the space group P21/n (PDF # 00-037-0719). This compound decomposes at $240\,^{\circ}$C generating a poorly crystalline phase corresponding to the cubic spinel (space group Fd-3 m). Then, from $350\,^{\circ}$C, this phase is progressively converted in the tetragonal spinel. Profile matching gives $a=0.574$ nm, $c=0.930$ nm and $D=16$ nm for the pattern recorded at $500\,^{\circ}$C.

The critical concentration of distorting Mn^{3+} required in the octahedral sites to trigger the Jahn–Teller effect is about 55% [41]. Thus the transient formation of the cubic spinel could be explained by the partial oxidation, after the oxalate decomposition, of more than 45% of Mn^{3+} into non-distorting Mn^{4+}. From $350\,^{\circ}$C Mn^{4+} cations are reduced in Mn^{3+} inducing the progressive conversion in the tetragonal spinel.

In the case of cobalt oxalate (lower-right plot) the dehydration occurs above $140\,^{\circ}$C, giving the monoclinic cobalt oxalate (PDF # 00-037-0719), which starts to decompose at $230\,^{\circ}$C to yield the cubic spinel Co_3O_4 (space group Fd-3m, PDF # 00-042-1467). Profile matching, for the pattern recorded at $300\,^{\circ}$C, gives $a=0.809$ nm and $D=12$ nm.

3.3. Characterization of oxides used as catalysts

3.3.1. XRD

Whatever the decomposition temperature of oxalates, the oxides used as catalysts were heated in air at $300\,^{\circ}$C for 1 h. The crystal structure, lattice parameter and crystallite size of these materials are reported in Table 3. As shown in the previous section, the oxides for which $x<0.9$ are amorphous. The XRD pattern of $Co_{0.9}Mn_{2.1}O_4$ shows very broad lines corresponding to a cubic spinel compound but is is too poorly crystallized to evaluate its cell parameter and crystallite size. For $x>0.9$ all the products have a cubic spinel structure. The cell parameters of the mixed oxides are slightly larger than the cell parameter of Co_3O_4. Neutron diffraction data on ceramics showed that, for $1<x<2$, the tetrahedral sites are fully occupied by Co^{2+} and the substitution now occurs in octahedral sites where Mn^{3+} is replaced both by Co^{2+} and Co^{3+} bearing in mind that each Co^{2+} also implies the oxidation of one Mn^{3+} in Mn^{4+} to preserve the global electro neutrality [40]. Because Co^{2+} and Mn^{3+} ions have a larger diameter (respectively, 79 and 72 pm)
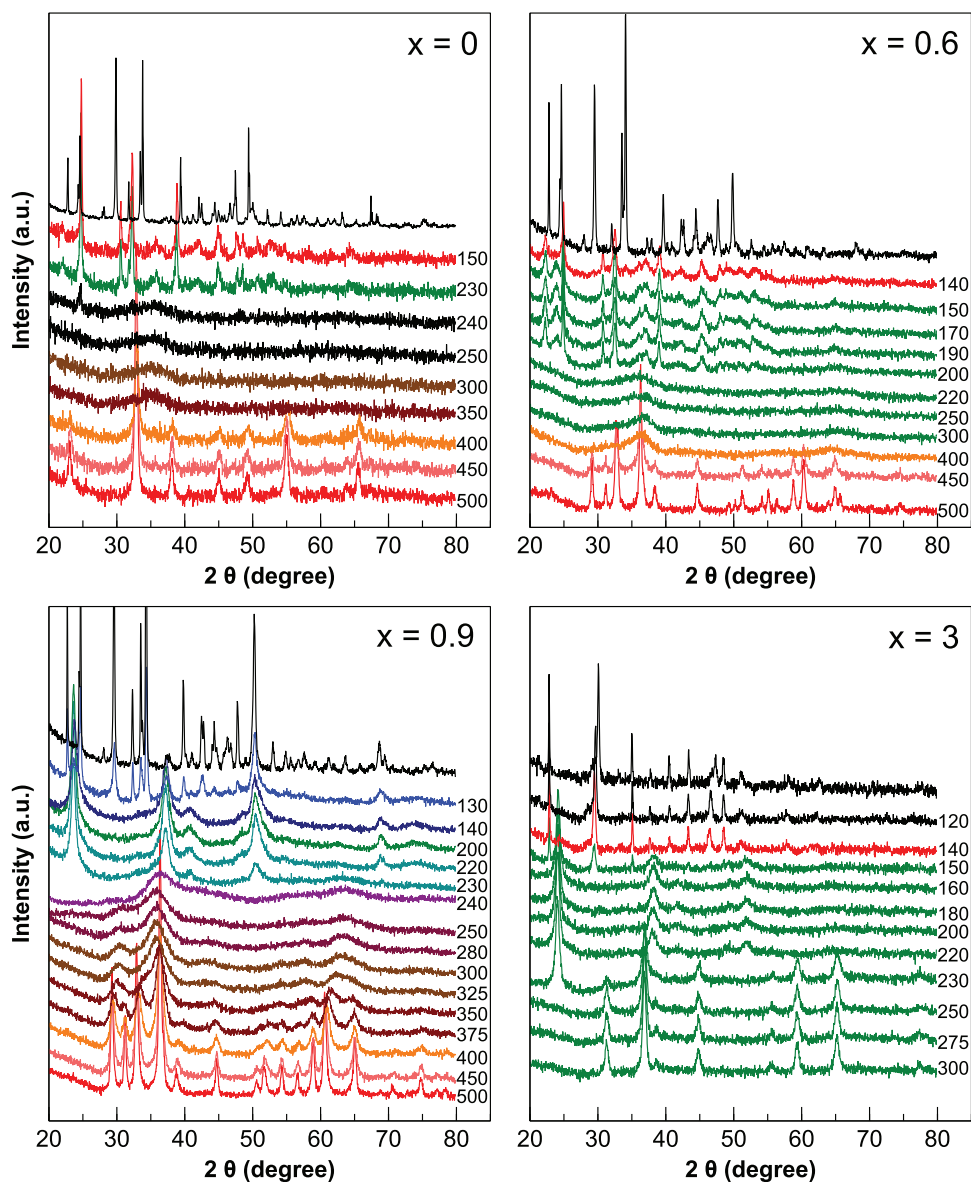
Fig. 5. XRD patterns recorded at increasing temperature during the decomposition of oxalates in air.

than LS Co^{3+} ions (55 pm) it is expected that the cell parameter of mixed oxides be larger than that of Co$_3$O$_4$. The biggest cell parameter is observed for $x=2$ probably because this oxide contains the largest amount of Co^{2+}. Furthermore the increase of cobalt content is associated with a significant growth of the crystallite.

3.3.2. Electron microscopy

At medium magnification, the SEM images of oxalates before and after decomposition are similar as shown in the case of Co$_{2.3}$Mn$_{0.7}$O$_4$ in Fig. 6 (left and center images). Thus, despite a mass loss close to 60%, when the reaction conditions allows con-

Table 3
Microstructural and textural properties of mixed oxides (Co$_x$Mn$_{3-x}$O$_4$) obtained after heating in air at 300 °C. Structural parameters was determined by profile fitting of XRD patterns with FULLPROF software [15]; D is the crystallite size. BET surface area (S_{BET}) and pore volume (V_{pore}) were calculated from N$_2$ adsorption isotherms at 77 K. The values of S_{BET} and V_{pore} are the average of several measurements.

x	Structure	a (nm)	D (nm)	S_{BET} (m^2/g)	C_{BET}	V_{pore} (cm^3/g)
0	Amorphous			90 ± 5	110	0.16 ± 0.01
0.6	Amorphous			100 ± 10	140	0.21 ± 0.02
0.9	Cubic spinel			230 ± 20	160	0.28 ± 0.03
1.6	Cubic spinel	8.11	6	270 ± 30	50	0.33 ± 0.04
2.0	Cubic spinel	8.12	7	260 ± 30	40	0.48 ± 0.05
2.3	Cubic spinel	8.10	9	220 ± 20	35	0.29 ± 0.03
3	Cubic spinel	8.09	16	60 ± 5	50	0.27 ± 0.01

Fig. 6. SEM images of $Co_{0.77}Mn_{0.23}C_2O_4.2H_2O$ oxalate (left image) and $Co_{2.3}Mn_{0.7}O_4$ oxide (middle image). TEM micrograph of $Co_{2.3}Mn_{0.7}O_4$ oxide (right image).

trolling the decomposition rate, the external shape of the oxalate particles is kept. It is possible on the central micrography to make out many cracks indicating that the oxide particles are highly fractured but the porosity is more easily evidenced on the TEM image which clearly shows the void between crystallites (right image). The crystallite size is in good agreement with the size obtained from XRD.

3.3.3. Specific surface area, pore volume and pore size distribution (PSD)

The BET specific surface areas (S_{BET}) and the pore volume (V_{pore}) of the materials heated at 300 °C, calculated from the N_2 adsorption isotherms, are reported in Table 3. In the case of mixed oxides, we observe that S_{BET} is strongly dependent of the decomposition conditions so that, for several preparations done in similar conditions, S_{BET} can differ by about 20%. Monometallic and amorphous oxides have the lowest surface and pore volume. The highest S_{BET} is obtained for $x \approx 2$; above this value the increase of cobalt content is associated with a diminution of the surface area and pore volume.

The high surface area and porosity of oxides strongly contrast with the low textural properties measured on oxalates (see Table 2). This large interface is created because there is almost no shrinkage of the oxalate particles induced by the big mass loss occurring during decomposition process.

Some representative isotherms and their associated PSD, calculated using NLDFT method, are plotted in Fig. 7. The porosity of these material spans a wide range, from micropores to macropores; however their PSD varies considerably according to the cobalt fraction. The approximate correlation between the crystallite size and the position of the main peak of PSD lets suppose that the mesopores correspond to the inter-crystallite spaces. The pores in the macropore range are probably due to the inter-granular porosity corresponding for example to the void between the particles.

3.4. Catalytic activity

The catalytic activity of the monometallic and mixed oxides, for CO and C_3H_8 total oxidation, is presented in Fig. 8. These measurements were not done at steady state but with a dynamic ramp rate of temperature (200 °C/h) and on-line monitoring using mass spectrometry. For CO oxidation, to reach the maximum activity, the catalysts were heated in a dry gas flow (20% O_2 in Ar). For propane oxidation this pre-treatment was not required to obtain optimum activity. We detected only CO_2 and H_2O as products of oxidation and the carbon balance was close to 100% within 2%. All the catalysts were tested over the temperature range (20 tests). Some representative CO (left) and C_3H_8 (right) conversion curves versus temperature (light-off curves) are shown on the upper plots of Fig. 8. We noticed that the same oxalate decomposed in what
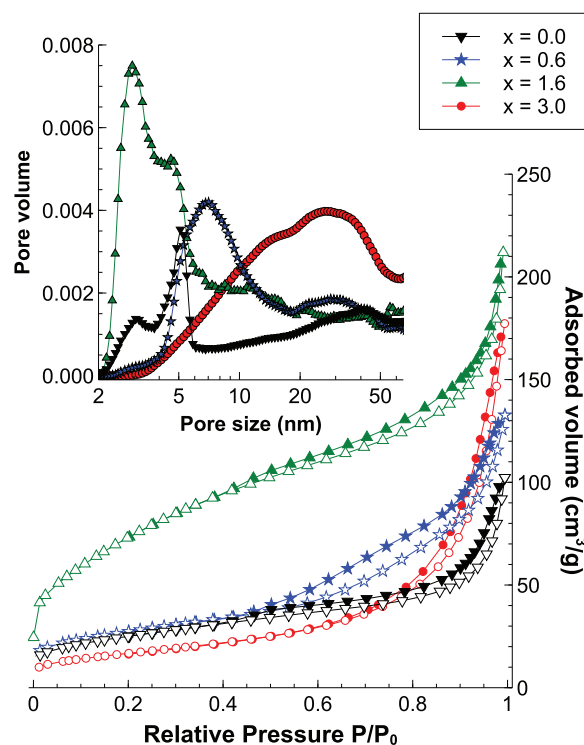

Fig. 7. N_2 adsorption-desorption isotherms and their associated pore size distribution (PSD) calculated using NLDFT method [18].

seems to be the same conditions could produce two catalysts having significant differences in activity. This is illustrated in the lower charts where the conversion observed at 60 °C for CO (left) and 200 °C for C_3H_8 (right) are plotted versus the amount of cobalt. Despite the scattering of the results, the effect of the substitution of manganese by cobalt seems rather similar for both reactions. Especially we observe that, for $x < 0.9$, the substitution does not change the activity whereas for $x = 0.9$ the activity is clearly better (about 3 times). Besides Co_3O_4 has a lower activity than $Co_{2.3}Mn_{0.7}O_4$ which seems to be the best composition.

The boost of activity for $x = 0.9$ is associated with a strong increase of S_{BET} which rises from 100 to 230 m^2/g. In an attempt to dissociate the effect of specific area from the influence of cobalt concentration, we calculated, from the conversion rate and S_{BET}, the intrinsic activity, A_i, defined as the number of reactant μmoles converted per second and per m^2 of catalyst. This intrinsic activity, plotted against the cobalt fraction, is shown in Fig. 9. In the case of CO oxidation A_i does not appear to be directly dependent of cobalt fraction below $x = 1.5$. Then a strong improvement of activ-
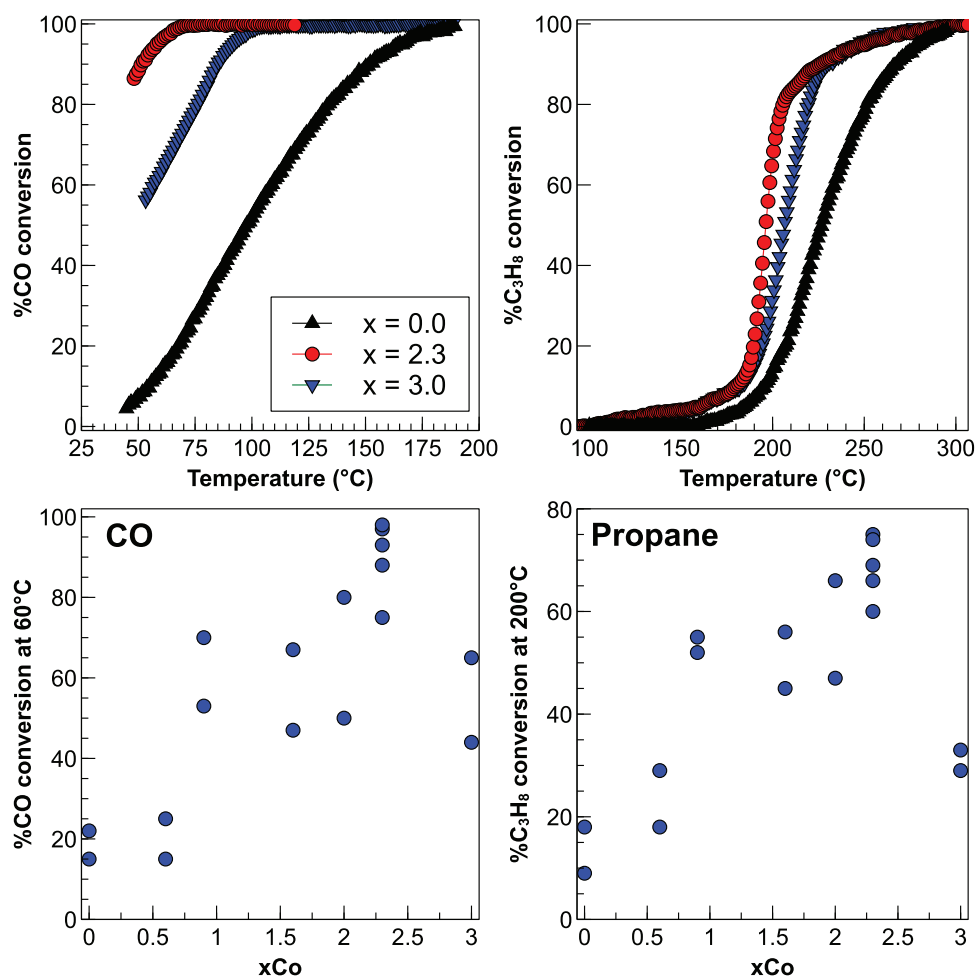
Fig. 8. Examples of the CO (upper-left) and C_3H_8 (upper-right) conversion curves versus temperature (light-off curves). Effect of cobalt fraction on the conversion observed at 60 °C for CO (lower-left) and 200 °C for C_3H_8 (lower-right).
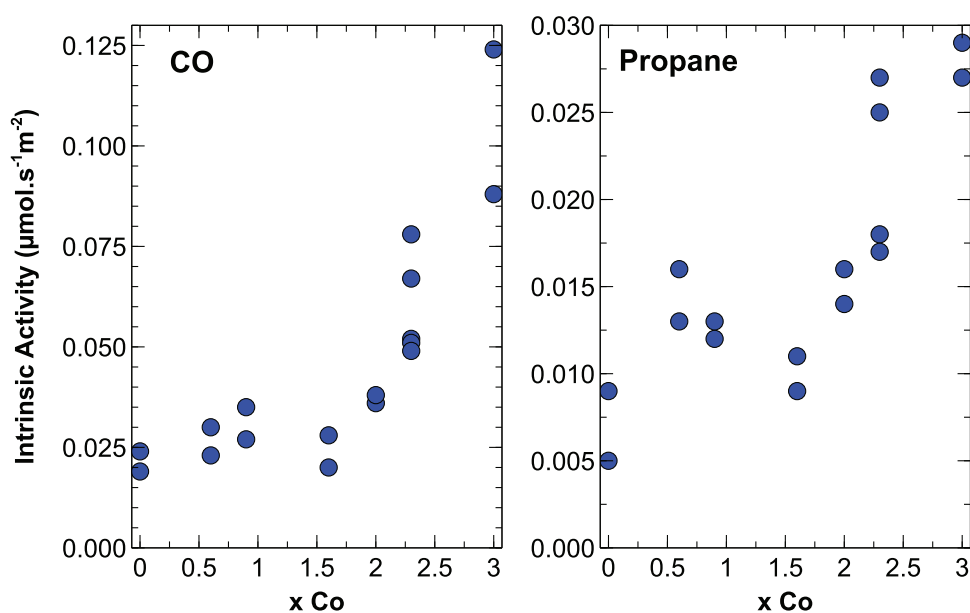

Fig. 9. Intrinsic activity plotted against the cobalt fraction for CO oxidation at 60 °C (left) and propane oxidation at 200 °C (right).
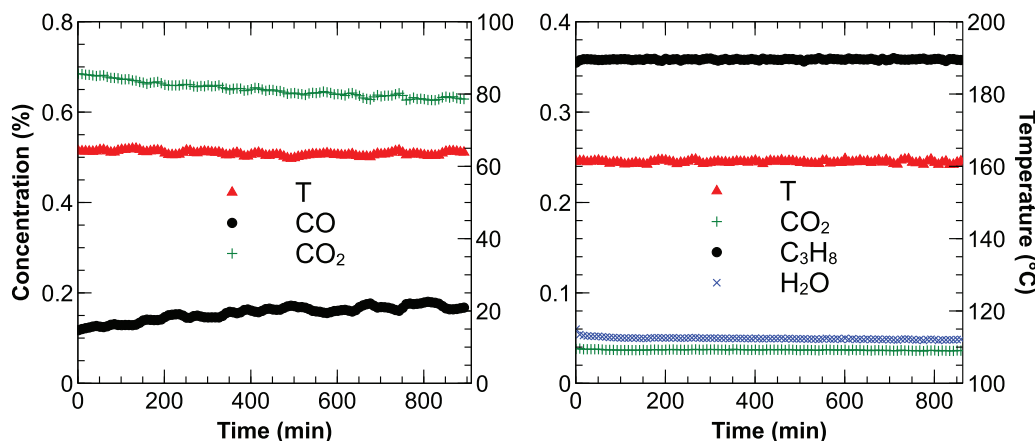
Figure 10. CO (left) and propane (right) conversion with time on stream for $Co_{2.3}Mn_{0.7}O_4$ catalyst.

Table 4
Comparison of catalyst activity for propane oxidation at 200 °C.

Ref.	Catalyst	Catalyst mass (g)	Flow rate (cm^3/min)	Inlet C_3H_8 concentration (%)	%C_3H_8 conv. at 175 °C	Activity at 175 °C(μmol s^{-1} g^{-1})
[49]	Co_3O_4	0.25	50	0.80	21	0.25
[50]	4%Au/Co_3O_4	0.25	50	0.80	32	0.38
[51]	Co_3O_4	0.05	98	0.37	5	0.27
this work	$Co_{2.3}Mn_{0.7}O_4$	0.05	98	0.37	8	0.43

ity is observed for higher cobalt content. For propane oxidation, a similar correlation between A_i and cobalt fraction is observed for $x > 1.5$. Below $x = 1.5$, the correlation is less clear.

Several works have demonstrated that the octahedral sites are almost exclusively exposed at the surface of the spinel oxides [43–45]. Moreover it was also shown that the catalytic activity of cobalt oxides was due to Co^{3+} ions in octahedral sites [45,46]. Hence, for low cobalt content, it is expected that the catalytic activity does not change much because the substitution occurs only in the inactive tetrahedral sites where Co^{2+} replaces Mn^{2+}. When the tetrahedral sites are fully occupied by Co^{2+} ($x > 1$) the substitution occurs in octahedral sites creating active Co^{3+} ions [40].

The apparent activation energy for propane oxidation was determined from Arrhenius plots in the conversion range 0–10%. Except for manganese oxide, it was found almost constant at 60 ± 10 kJ/mol whatever the cobalt concentration. For MnO_x the activation energy is slightly higher at 75 ± 10 kJ/mol.

In the case of the CO oxidation the conversion is too high to allow the calculation of activation energy.

For the best catalyst ($Co_{2.3}Mn_{0.7}O_4$) we followed the effect of the oxalate decomposition temperature (in the range 220–300 °C) on the catalytic activity for propane oxidation. Although the variations in activity were of the same order of magnitude as the differences between replicates it seems that the optimum decomposition temperature is 280 °C.

The long-term stability of the conversion was tested with the best catalyst ($Co_{2.3}Mn_{0.7}O_4$). The left plot of Fig. 10 shows that the CO conversion decreases by about 8% during the first half of the test. Then it seems to remain stable until the end of the test. Unexpectedly we observed variations of temperature associated with variations of conversion. We could not determine if it was the temperature change that induced conversion change or the converse. As regards propane oxidation, the right plot of Fig. 10 indicates that the conversion was stable for more than 14 h at 160 °C.

To compare the catalytic activity of our materials with the data reported in the literature we calculated the specific activity defined as the number of reactant μmoles converted per second and per gram of catalyst.

As it was demonstrated that CO conversion was strongly dependent upon the amount of water in the inlet gas [46–48] we limited our comparison to propane oxidation. This comparison revealed (Table 4) that $Co_{2.3}Mn_{0.7}O_4$ activity was more than 50% higher than that of Co_3O_4 catalysts found in the most recent publications and was similar to catalysts for which precious metal have been added to enhance the activity.

4. Conclusion

Cobalt-manganese mixed oxalate dihydrates crystallize in the monoclinic structure when the cobalt fraction is lower than 0.5 and in orthorhombic structure otherwise. The controlled decomposition of these oxalates near 200 °C, followed by a calcination at 300 °C, strongly restrains the shrinkage of particles and the crystallite sintering, producing mixed oxides $Co_xMn_{3-x}O_4$ with a very large surface area. For $x < 0.9$ these materials are amorphous. For $x \geq 0.9$ they have a cubic spinel structure and their crystallite size increases with the cobalt fraction.

These spinel oxides exhibit an outstanding catalytic activity for propane oxidation. They are also active for CO oxidation even at ambient temperature. This high activity is correlated both with the surface area and the cobalt concentration. For manganese oxide the apparent activation energy for propane oxidation is 75 ± 10 kJ/mol whereas it is 60 ± 10 kJ/mol and nearly independent of cobalt fraction for the other catalysts. The most efficient material is $Co_{2.3}Mn_{0.7}O_4$, which has an activity more than 50% higher than the best Co_3O_4 catalysts reported in the literature.

References

[1] L.F. Liotta, Catalytic oxidation of volatile organic compounds on supported noble metals, Appl. Catal. B: Environ. 100 (2010) 403–412.

[2] M. Ousmane, L.F. Liotta, G. Carlo, Di, G. Pantaleo, A.M. Venezia, G. Deganello, L. Retailleau, A. Boreave, A. Giroir-Fendler, Supported Au Catalysts For Low-Temperature Abatement of Propene and Toluene, As Model VOCs: Support Effect, Appl. Catal. B: Environ. 101 (2011) 629–637.

[3] V.P. Santos, S.A.C. Carabineiro, P.B. Tavares, M.F.R. Pereira, J.J.M. Orfao, J.L. Figueiredo, Oxidation of CO, ethanol and toluene over TiO₂ supported noble metal catalysts, Appl. Catal. B: Environ. 99 (2010) 198–205.

[4] M.J. Patterson, D.E. Angove, N.W. Cant, The effect of carbon monoxide on the oxidation of four C6–C8 hydrocarbons over platinum, palladium and rhodium, Appl. Catal. B: Environ. 26 (2000) 47–57.

[5] P. Marecot, A. Fakche, B. Kellali, G. Mabilon, P. Prigent, J. Barbier, Propane and propene oxidation over platinum and palladium on alumina: effects of chloride and water, Appl. Catal. B Environ. 3 (1994) 283–294.

[6] G. Busca, M. Daturi, E. Finocchio, V. Lorenzelli, G. Ramis, R.J. Willey, Transition metal mixed oxides as combustion catalysts: preparation, characterization and activity mechanisms, Catal. Today 33 (1997) 239–249.

[7] S. Royer, D. Duprez, Catalytic oxidation of carbon monoxide over transition metal oxides, ChemCatChem 3 (2011) 24–65.

[8] B. Solsona, I. Vazquez, T. Garcia, T.E. Davies, S.H. Taylor, Complete oxidation of short chain alkanes using a nanocrystalline cobalt oxide catalyst, Catal. Lett. 116 (3–4) (2007) 116–121.

[9] J. Zhu, Qiuming Gao, Mesoporous MCo₂O₄ (M = Cu, Mn and Ni) spinels: structural replication, characterization and catalytic application in CO oxidation, Micropor. Mesopor. Mater. 124 (2009) 144–152.

[10] S. Todorova, H. Kolev, J.P. Holgado, G. Kadinov, Ch. Bonev, R. Pereniguez, A. Caballero, Complete *n*-hexane oxidation over supported Mn–Co catalysts, Appl. Catal. B: Environ. 94 (2010) 46–54.

[11] B. Puertolas, A. Smith, I. Vazquez, A. Dejoz, A. Moragues, T. Garcia, B. Solsona, The different catalytic behaviour in the propane total oxidation of cobalt and manganese oxides prepared by a wet combustion procedure, Chem. Eng. J. 229 (2013) 547–558.

[12] C. Drouet, P. Alphonse, Synthesis of mixed manganites with high surface area by thermal decomposition of oxalates, J. Mater. Chem. 12 (2002) 3058–3063.

[13] V. Iablokov, K. Frey, O. Geszti, N. Kruse, High catalytic activity in CO oxidation over MnOₓ nanocrystals, Catal. Lett. 134 (2010) 210–216.

[14] J. Robin, Etude des oxalates métalliques premières pour la preparation de solution solides d'oxydes, Bulletin de la Société Chimique de France 20 (1953) 1078–1084.

[15] J. Rodríguez-Carvajal, Recent developments of the program FULLPROF, Commission on powder diffraction (IUCr) Newsletter 26, 12–19.

[16] P. Thompson, D.E. Cox, J.B. Hastings, Rietveld refinement of Debye-Scherrer synchrotron X-ray data from Al₂O₃, J. Appl. Crystallogr. 20 (1987) 79–83.

[17] S. Brunauer, P. Hemmett, E. Teller, Adsorption of gases in multimolecular layers, J. Am. Chem. Soc. 60 (1938) 309–319.

[18] N. Seaton, J. Walton, N. Quirke, A new analysis method for the determination of the pore size distribution of porous carbons from nitrogen adsorption measurements, Carbon 27 (1989) 853–861.

[19] D. Dollimore, D. Nicholson, The thermal decomposition of oxalates: part I, Var. Surf. Area Temp. Treat. Air J. Chem. Soc. 96 (1962) 0–96.

[20] D. Broadbent, D. Dollimore, J. Dollimore, The thermal decomposition of oxalates. part VII. The effect of prior dehydration conditions upon the subsequent decomposition of cobalt oxalate, J. Chem. Soc. A. (1966) 1491–1493.

[21] D. Dollimore, J. Dollimore, J. Little, The thermal decomposition of oxalates. Part X. Nitrogen adsorption data on solid residues from the isothermal heat treatment of manganese(II) oxalate dihydrate, J. Chem. Soc. A. (1969) 2946–2951.

[22] M.E. Brown, D. Dollimore, A.K. Galwey, Thermal decomposition of manganese(II) oxalate in vacuum and in oxygen, J. Chem. Soc. Faraday Trans. 1 70 (1974) 1316–1324.

[23] K. Nagase, K. Sato, N. Tanaka, Thermal dehydration and decomposition reactions of bivalent metal oxalates in the solid state, Bull. Chem. Soc. Jpn. 48 (1975) 439–442.

[24] J. Mu, D.D. Perlmutter, Thermal decomposition of carbonates, carboxylates, oxalates, acetates formates and hydroxides, Thermochim. Acta 49 (1981) 207–218.

[25] D. Dollimore, The thermal decomposition of oxalates. A review, Thermochim. Acta 117 (1987) 331–363.

[26] X. Gao, D. Dollimore, The thermal decomposition of oxalates. Part 26. A kinetic study of the thermal decomposition of manganese(II) oxalate dihydrate, Thermochim. Acta 215 (1993) 47–63.

[27] A. Coetzee, M.E. Brown, D.J. Eve, C.A. Strydom, Kinetics of the thermal dehydrations and decompositions of some mixed metal oxalates, J. Therm. Anal. 41 (1994) 357–385.

[28] A.K.H. Nohman, H.M. Ismail, G.A.M. Hussein, Thermal and chemical events in the decomposition course of manganese compounds, J. Anal. Appl. Pyrolysis 34 (2) (1995) 265–278.

[29] A.K. Nikumbh, A.E. Athare, S.K. Pardeshi, Thermal and electrical properties of manganese (II) oxalate dihydrate and cadmium (II) oxalate monohydrate, Thermochim. Acta 326 (1999) 187–192.

[30] M. Maciejewski, E. Ingier-Stocka, W.D. Emmerich, A. Baiker, Monitoring of the gas phase composition: a prerequisite for unravelling the mechanism of decomposition of solids. Thermal decomposition of cobalt oxalate dihydrate, J. Therm. Anal. Calorim. 60 (2000) 735–758.

[31] B.V. L'vov, Kinetics and mechanism of thermal decomposition of nickel, manganese, silver, mercury and lead oxalates, Thermochim. Acta 364 (2000) 99–109.

[32] B. Malecka, E. Drozdz-Cielsa, P.K. Olszewski, Kinetics of thermal decomposition of manganese(II) oxalate, J. Therm. Anal. Calorim. 74 (2003) 485–490.

[33] M.A. Mohamed, A.K. Galwey, S.A. Halawy, A comparative study of the thermal reactivities of some transition metal oxalates in selected atmospheres, Thermochim. Acta 429 (2005) 57–72.

[34] B. Donkova, D. Mehandjiev, Mechanism of decomposition of manganese(II) Oxalate dihydrate and manganese(II) oxalate trihydrate, Thermochim. Acta 421 (2004) 141–149.

[35] M.E. Brown, D. Dollimore, A.K. Galwey, Thermochemistry of decomposition of manganese(II) oxalate dihydrate, Thermochim. Acta 21 (1977) 103–110.

[36] V. Iablokov, K. Frey, O. Geszti, N. Kruse, High catalytic activity in CO oxidation over MnOₓ nanocrystals, Catal. Lett. 134 (2010) 210–216.

[37] N.B.S. The, Tables of chemical thermodynamic properties, J. Phys. Chem. Ref. Data 11 (supplement no. 2) (1982).

[38] O. Kubaschewski, C.B. Alcock, P.J. Spencer, Materials Thermochemistry, 6th ed., Pergamon Press, 1993.

[39] Y. Xiao, D.E. Wittmer, F. Izumi, S. Mini, T. Graber, P.J. Viccaro, Determination of cations distribution in Mn₃O₄ by anomalous X-ray powder diffraction, Appl. Phys. Lett. 85 (2004) 736–738.

[40] H. Bordeneuve, C. Tenailleau, S. Guillemet-Fritsch, R. Smith, E. Suard, A. Rousset, Structural variations and cation distributions in Mn₃₋ₓCoₓO₄ (0 < x <3) dense ceramics using neutron diffraction data, Solid State Sci. 12 (2010) 379–386.

[41] D. Jarosch, Crystal structure refinement and reflectance measurements of hausmannite, Mn₃O₄, Mineral. Petrol. 37 (1987) 15–23.

[42] C. Laberty, M. Verelst, P. Lecante, P. Alphonse, A. Mosset, A. Rousset, A wide angle X-ray scattering (WAXS) study of nonstoichiometric nickel manganite spinels NiMn₂□₃δ/₄O₄₊δ, J. Solid State Chem. 129 (1997) 271–276.

[43] M. Shelef, M.A.Z. Wheeler, H.C. Yao, Ion scattering spectra from spinel surfaces, Surf. Sci. 47 (1975) 697–703.

[44] J.P. Jacobs, A. Maltha, J.G.H. Reintjes, J. Drimal, V. Ponec, H.H. Brongersma, The surface of catalytically active spinels, J. Catal. 147 (1994) 294–300.

[45] K. Omata, T. Takada, S. Kasahara, M. Yamada, Active site of substituted cobalt spine1 oxide for selective oxidation of CO/H₂. Part II, Appl. Cata. A: Gen. 146 (1996) 255–267.

[46] X. Xie, Y. Li, Z.Q. Liu, M. Haruta, W. Shen, Low-temperature oxidation of CO catalysed by Co₃O₄ nanorods, Nature 458 (2009) 746–749.

[47] Y.F. Yu Yao, The oxidation of hydrocarbons and CO over metal oxides: III. Co₃O₄, J. Catal. 33 (1974) 108–122.

[48] F. Grillo, M.M. Natile, A. Glisenti, Low temperature oxidation of carbon monoxide: the influence of water and oxygen on the reactivity of a Co₃O₄ powder surface, Appl. Catal. B: Environ. 48 (2004) 267–274.

[49] T. Garcia, S. Agouram, J.F. Sanchez-Royo, R. Murillo, A.M. Mastral, A. Aranda, I. Vazquez, A. Dejoz, B. Solsona, Deep oxidation of volatile organic compounds using ordered cobalt oxides prepared by a nanocasting route, Appl. Cata. A: Gen. 386 (2010) 16–27.

[50] B. Solsona, E. Aylon, R. Murillo, A.M. Mastral, A. Monzonis, S. Agouram, T.E. Davies, S.H. Taylor, T. Garcia, Deep oxidation of pollutants using gold deposited on a high surface area cobalt oxide prepared by a nanocasting route, J. Hazard. Mater. 187 (2011) 544–552.

[51] G. Salek, P. Alphonse, P. Dufour, S. Guillemet-Fritsch, C. Tenailleau, Low-temperature carbon monoxide and propane total oxidation by nanocrystalline cobalt oxides, Appl. Catal. B: Environ. 147 (2014) 1–7.